

Dawsonite and ankerite formation in the LDX-1 structure, Yinggehai basin, South China Sea: An analogy for carbon mineralization in subsurface sandstone aquifers

Lei Yu^{a, b}, Keqiang Wu^c, Li Liu^{a, *}, Na Liu^a, Xiaoran Ming^d, Eric H. Oelkers^{b, e, *}

a. College of Earth Sciences, Jilin University, 130061 Changchun, PR China

b. Department of Earth Sciences, University College London, Gower Street, WC1E 6BT London, United Kingdom

c. China National Offshore Oil Corporation (CNOOC) Research Institute, 100028 Beijing, China

d. The First Monitoring and Application Center, China Earthquake Administration, Tianjin, 300180, China

e. GET-Université de Toulouse-CNRS-IRD-OMP, 14 Avenue Edouard Belin, 31400 Toulouse, France

Abstract

The geochemistry and petrology of the LDX-1 structure of the Yinggehai basin, a natural analog of a sedimentary carbon storage site, was investigated to understand the consequences of the charging of CO₂ gas in this system. The rocks in this structure are dominated by subarkose and sublitharenite sandstones. The authigenic minerals formed after CO₂ injection are dawsonite, microcrystalline quartz, kaolinite and ankerite. Dawsonite and ankerite are formed just beneath a CO₂ bearing anticlinal structure due to the reactions between silicate minerals (feldspars and clay minerals) and the fluid phase. Carbon and oxygen isotopic analyses indicate that the main carbon source for dawsonite and ankerite formation was mantle magmatic CO₂. The aqueous activities of sodium and calcium, the partial pressure of CO₂, pH and temperature are the key factors influencing the stability of the dawsonite and ankerite. The presence of the anticlinal structure maintaining a locally high CO₂ partial pressure in the waters beneath this structure is likely responsible for the observed long-term persistence of dawsonite and ankerite in this system.

Keywords: authigenic carbonate minerals, carbon and oxygen isotopes, dawsonite stability, carbon capture and storage (CCS), Yinggehai Basin

1 Introduction

Carbon-dioxide emissions to the atmosphere by anthropogenic industrial activities are a key factor causing global climate change (IPCC, 2005, 2007; Manabe and Stouffer, 1993). The injection of anthropogenic CO₂ into deep geologic formations has been advocated to slow increasing atmospheric CO₂ concentrations and its effect on global climate (Bachu et al., 1994; Bachu, 2003; IPCC, 2005, 2007; Oelkers and Cole, 2008). There are four mechanisms of carbon storage in the subsurface: structural and stratigraphic trapping, residual CO₂ trapping, solubility trapping and mineral trapping (IPCC, 2005; Johnson et al., 2001). Of these, mineral trapping, and in particular in-situ carbon mineralization, is the most stable and safe carbon storage solution (Lackner et al 1995; Johnson et al., 2001; Matter et al., 2016; Oelkers et al., 2008; Power et al. 2013).

Sandstone aquifers with impermeable cap-rocks are commonly considered for carbon storage as they have adequate permeability and pore space, and are abundant in the subsurface (Benson and Cole, 2008; IPCC, 2005; Xu et al., 2005). A number of studies have shown that calcite, siderite, magnesite, dolomite, ankerite and dawsonite could form in various sandstones in response to CO₂ injection. (Baker et al., 1995; Fischer et al., 2010; Gao et al., 2009; Gaus et al., 2005; Hellevang et al., 2013; Higgs et al., 2013, 2015; Hitchon, 1996; Klajmon et al., 2017; Liu et al., 2011; Moore et al., 2005; Pauwels et al., 2007; Pearce et al., 2016; Pham et al., 2011; Uysal et al., 2011; Van Pham et al., 2012; Worden, 2006; Xu et al., 2004, 2005, 2007, 2010; Yu et al., 2015; Zhao et al., 2018; Zhou et al., 2014). Of these minerals, dawsonite (NaAl(OH)₂CO₃) is particularly attractive as a carbon storage host as it contains sodium and aluminum, which can be abundant in sedimentary silicates. This mineral, however, is more reactive and less stable than many of the aforementioned divalent

metal carbonate minerals (Bénézeth et al., 2007; Hellevang et al., 2005, 2011).

The LDX-1 structure in the Yinggehai basin of South China Sea provides an insightful analogy for the study of mineral carbonation in sandstone aquifers (Fig. 1). The gas phase in the LDX-1 structure contains as much as 93 volume percent CO₂ and this CO₂ has a distinct inorganic carbon isotopic signature (He et al., 2005; Huang et al., 2003). In addition, past studies concluded that the CO₂ gas injection into this structure occurred after that of the hydrocarbon gases (Huang et al., 2004; Sun and Wang, 2000), which is similar to scenarios that might be encountered by injecting into former oil field reservoirs.

The purpose of this study is to characterize the mineralogy and paragenesis in two wells drilled into the LDX structure to investigate sandstone diagenesis and carbonate mineral formation in response to the influx of CO₂. Results will be used to gain further insight into the potential for mineral carbonation in sedimentary sandstones as part of subsurface carbon storage efforts.

2 Geological setting

The Yinggehai basin, which developed during the Cenozoic, is a natural gas-rich rift basin. It is located between the Indian and South China plate, formed by the combination of lithosphere extension and the deep, strike-slip Red River fault. The direction of this basin is Northwest-Southeast, with a total area of approximately 11×10^4 km² (Huang et al., 2009; Wan et al., 2007; Fig. 1a, b). Two northwest-trending, deep-to-basement faults divide the Yinggehai basin into three sub-structural units: The Central Depression, the Ying Dong Slope and the Ying Xi Slope (see Fig 1). The central depression consists of two tectonic units: the Lin Gao uplift and the diapir structure belt (Fig 1b; Zhu et al., 2004). During the Miocene, the Yinggehai basin was filled with argillaceous sediments along the fault and formed a series of diapir structures in the central depression zone (Huang et al., 2009). He et al. (2005) reported that most of the natural gas reservoirs with high CO₂ contents are concentrated in these diapir

structures.

The basement of the Yinggehai basin is dominated by palaeozoic magmatic rocks (Hao et al., 1998). According to the drilling strata, the Cenozoic sediments include the Eocene Lingtou Formation, the Oligocene Yacheng and Lingshui Formations, the Miocene Sanya, Meishan, and Huangliu Formations, the Pliocene Yinggehai Formation and the Quaternary Ledong Formation. The thickness of the Cenozoic sediments in this basin is up to 16-17 km (Gong et al., 1997; Huang et al., 2004, 2009; Meng et al., 2012; Zhu et al., 2007) (Fig. 2). The Lingtou Formation mainly consists of sandstone and mudstone. The Yacheng and Lingshui Formations are composed of mudstone and silty mudstone interbedded with mudstone. Both the Sanya and Meishan Formations are dominated by calcareous mudstone. The Huangliu, Yinggehai and Ledong Formations are mainly siltstone, sandstone and interbedded mudstone. The Miocene mudstone is the main source rock of natural gas in this basin, while the interbedded mudstone and sandstone of the overlying Huangliu and Yinggehai Formations provide a good reservoir and cap rock system for the basin (Wang and Huang, 2008). According to the logging data, the Yinggehai and Huangliu formations contain the main CO₂ gas reservoirs in the basin.

The LDX-1 Structure is a dome structure located in the southeast of the Ledong area in the central depression of the Yinggehai Basin (Fig. 1b). The gas reservoir in the LDX-1 structure is an anticline formed by a mud diapir. The rocks containing the CO₂-rich gas reservoirs consist mainly of the marine sandstones of the Pliocene Yanggehai Formation (Fig. 2) and are located at a depth of 392 m to 2300 m (Huang et al., 2004; Li et al., 2005). According to gas measurements, the LDX-1 reservoirs are dominated by hydrocarbon gas and CO₂; the CO₂ content ranges from 41.9% to 78.7% (Huang et al., 2004).

There were two major episodes of gas emplacement into the Yinggehai basin, the first from an organic source and dominated by CH₄ and the second from an inorganic sourced and dominated by CO₂. According to the Xie et al., (2014), the arrival of the

CH₄ dominated gas was at approximately 3.7 Ma. The CO₂ dominated gas arrived later. Estimates of its arrival time range from 0.3 to 1.9 Ma (Fu et al., 2016; Huang et al., 2005; Wang et al., 2004; Xie et al., 2014). As such this basin provides a close natural analogue to the filling of a former hydrocarbon reservoir with CO₂ as part of subsurface carbon storage efforts.

3 Sampling and research methods

A total 159 sandstone samples were collected from the gas reservoir layers of the LDX-1 structure of the Yinggehai Formation. The samples were collected from the depths of 1841.62 to 1869.02 m (from well LDX-1-1) and of 1958.07 to 1905.13 m (from well LDX-1-4). The compositions of the sandstone samples were determined by counting 300 points in each thin section following the approach of Dickson (1965) using an OLYMPUS BX51 polarizing microscope. To identify the carbonate minerals, all the thin sections were stained with Alizarin Red S and K-ferricyanide solutions following the procedure of Dickson (1965). Authigenic mineral observations and energy spectrum analyses were performed at the Research Center of Paleontology and Stratigraphy of Jilin University, using a JEOL JSM-6700F scanning electron microscope (SEM), equipped with energy dispersive X-ray spectrometer (EDS) analyzer manufactured by Oxford, UK; mineral surfaces were gold coated prior to this analysis.

Based on a systematic petrographic study of the sandstone in the gas reservoirs, 10 dawsonite-bearing samples were selected for carbon and oxygen isotope analyses using MAT253 isotopic ratio mass spectrometers at the Analytical Laboratory of The China National Nuclear Corporation (CNNC) Beijing Research Institute of Uranium Geology. The analytical method for obtaining stable isotopic compositions is based on past studies such as Liu et al. (2011). Samples were grounded into a powder using an agate mortar and pestle. The ground powers were sieved and the > 74 μm fraction was collected, then dried for 2 h at 105 °C under atmospheric pressure, to remove potential

surface volatile phases, before analyzing. For carbon and oxygen isotope analyses, 99% phosphoric acid (produced by Merck KGaA, Darmstadt, Germany) was reacted with crushed whole rock powders at 25 °C or 50 °C (McCrea, 1950). For dawsonite analysis, CO₂ released from samples during the first 4 h reactions at 25 °C was discarded, as this gas likely originated from the decomposition of calcite. After that, the reaction was continued for another 24h and the CO₂ was collected for the analysis of dawsonite isotopic compositions (Becker, 1971; Rosenbaum and Sheppard, 1986; Sharma and Clayton, 1965). For ankerite analysis, the CO₂ released during the first 24 h reaction at 25 °C was discarded, as it likely originated from calcite and dawsonite decomposition, then the reaction temperature was raised to 50 °C followed by the collection of the CO₂ produced by the decomposition reaction during subsequent 48 h (Uysal et al., 2011). The precision of the analyses is ±0.1‰ for δ¹³C and ±0.2‰ for δ¹⁸O. All reported isotope values in this study are relative to the Belemnite americana from the Peedee Formation (PDB) standard for carbon and Standard Mean Ocean Water (SMOW) for oxygen.

All the speciation and solubility calculations were conducted using PHREEQC v. 3 (Parkhurst and Appelo, 2013) with its Lawrence Livermore National Laboratory (LLNL) thermodynamic database after adding to it the stability constant for ankerite. The stability of ankerite in this study is based on the formula (Ca(Fe_{0.5}Mg_{0.5})(CO₃)₂) (see below). Its thermodynamic properties were estimated from the stoichiometrically weighted sum of the calcite, siderite and magnesite stability constants (Xu et al., 2004). The thermodynamic properties required for this estimate were calculated using the SUPCRTBL database (Zimmer et al., 2016). The resulting ankerite equilibrium constant and enthalpy of reaction are 0.642 and -69.326 kJ/mol at 70 °C and -0.087 and -77.803 kJ/mol 100 °C. Thermodynamic properties in the LLNL database are consistent with those of dawsonite reported by Bénézech et al. (2007). The Truesdell-Jones equation was used to calculate aqueous activity coefficients and the fugacity for CO₂ gas was calculated using the ThermoSolver 1.0 software (Barnes,

2006).

4 Results

4.1 Petrographic characteristics

The dawsonite in the LDX-1 structure is hosted in fine-grained subarkose and lithic quartz sandstones. The observed detrital minerals are mainly quartz (16.7% to 64.7%), feldspar (up to 12.0%) and rock fragments (up to 23.0%). The modal compositions of the detrital minerals are shown schematically in Fig 3. The feldspar is mainly comprised of plagioclase and also contains small amounts of orthoclase and perthite. The rock fragments mainly consist of metamorphic debris (up to 19%), granite debris (up to 8%), and sedimentary debris (up to 7%).

4.2 Authigenic mineralogy and paragenesis

The authigenic minerals observed in the rock samples are dawsonite, quartz, siderite, dolomite, ankerite, mixed-layer clays consisting of illite and smectite, and kaolinite.

4.2.1 Dawsonite

Dawsonite is principally found at depths of 1841.27 to 1867.23 m in well LDX-1-1 and 1863 to 2018 m in well LDX-1-4 with its content ranging from 0.2 to 6 Vol% as determined by point counting (see above). Dawsonite aggregates nucleate as microcrystalline grains then grow radially outward into the sandstone pores. Dawsonite growth usually terminates at the edge of the detrital minerals (eg. quartz and feldspar). Dawsonite could also be observed growing on dolomite (Fig. 4a, b), potassium feldspar and plagioclase (Fig 4c, d). The EDS results show that the dawsonite mainly consists of carbon, oxygen, sodium and aluminum having weight percents of 7.25 to 22.23, 50.43 to 66.93, 3.58 to 14.69, and 7.27 to 30.26 respectively (see Table 1).

4.2.2 Authigenic quartz

Two kinds of authigenic quartz were observed: quartz overgrowths and microcrystalline quartz. The content of authigenic quartz is low, generally less than 0.5%. Quartz overgrowths are the among the earliest authigenic silicate minerals observed and are evident due to clay rims between detrital quartz and these overgrowths. The thickness of the quartz overgrowths ranges from 0.01 to 0.06 mm. Furthermore, we observed some radial dawsonite surrounded by quartz overgrowths (see Fig. 4e), suggesting some of the quartz precipitated concurrently with or after the dawsonite. In addition, SEM images show that the microcrystalline quartz was distributed in sandstone pores sporadically and is associated with kaolinite. This kaolinite is also associated with dawsonite in some places (Fig. 4f). Such observations further suggest that the microcrystalline quartz formed during same time period as the dawsonite.

4.2.3 Siderite

Most siderite was distributed in pores as subhedral intergranular crystals or aggregates along the boundaries of the detrital grains (Fig. 4g). The content of the siderite ranges from 0.5% to 13.5% in the bulk rock and the crystal sizes range from 0.01 mm to 0.03 mm. The color of the siderite is yellow brown to dark brown under single polarized light. The siderite crystals were distributed either in the inner side of quartz overgrowth or near the clay rims surrounding the original quartz grain boundaries, indicating that siderite formation was earlier than or concurrent with the quartz overgrowths.

4.2.4 Dolomite

The dolomite content (0.5 to 43 Vol%) varied substantially in the studied cores. As dolomite is not stained by Alizarin Red S and K-ferricyanide solutions, it is readily

distinguished from other carbonates. Under the polarizing microscope, some dolomite was observed being replaced by dawsonite aggregates (Fig. 4h). SEM analysis revealed that the ends of some needle-like dawsonite crystals terminate at the faces of dolomite crystals exhibiting a “bridged phenomenon” (Figure 4a, b). Both sets of observations imply that the dolomite formed earlier than the dawsonite, yet the presence of some detrital dolomite cannot be discounted.

4.2.5 Ankerite

Ankerite (0.5 to 36 Vol%) mainly surrounds dolomite crystals as rim-like growths (Fig. 4i) or as euhedral to subhedral intergranular crystals (Fig. 4j, k). Under the Back Scattered Electron (BSE) mode, the ankerite is seen to form of nearly equal ring-like shapes along the dolomite surfaces as it replaced this mineral. Some ankerite is seen to have grown on dawsonite (Fig 4j, k). Such observations suggest that ankerite formation occurred later than both the dolomite and dawsonite. EDS analyses results for ankerite showed that its Ca, Mg, and Fe content ranged from 0.39 to 9.22, 2.4 to 6.52, and 1.47 to 7.82 atomic percent respectively (see Table 2), consistent with the formula $\text{Ca}(\text{Fe}_{0.5}\text{Mg}_{0.5})(\text{CO}_3)_2$.

4.2.6 Clay minerals

The XRD results indicate that the clay minerals in the CO₂-containing reservoirs of the Yinggehai Basin mainly consist of mixed-layer illite and smectite, and kaolinite (Huang et al., 2004; Jiang et al., 2015; Tong et al., 2012). The mixed layer illite and smectite commonly surround the detrital minerals as “clay rims”, which could be identified by polarizing microscope. Mixed layer illite and smectite are not found in the sandstone pores, suggesting that it is the earliest formed secondary mineral in the diagenetic sequence. Honeycomb-like authigenic clay is seen to grow on K-feldspar (see Fig. 4l, m). According the EDS results shown in Table 3, most of the smectite and mixed layer illite are Ca depleted. This suggests that the Ca in the smectite and mixed

layer of illite and smectite may have been removed over time through water-mineral reactions.

Authigenic kaolinite grows as vermicular assemblages in the sandstone pores. Hexagonal kaolinite crystals are found attached to dawsonite crystals (Fig. 4n), at times adjacent to small "etch pits" on the dawsonite surface (Fig. 4o), suggesting that some kaolinite post-dates the dawsonite. However, vermicular kaolinite is commonly interspersed between acicular dawsonite crystals, suggesting that this kaolinite formed slightly earlier than or concurrently with dawsonite (Fig. 4p). In some places ankerite grew on the top of kaolinite aggregates (Fig. 4q). This suggests that the formation of kaolinite might have spanned from the period from when dawsonite grew through that of ankerite formation.

Chlorite was not observed in the samples considered in this study. Its presence in the rocks of the LDX system was reported by Fu et al. (2016). Moreover, the presence of chlorite within and below the CO₂ gas reservoirs is inferred as a potential source of the iron leading to ankerite precipitation (see below).

4.3 Vertical characteristics of authigenic carbonates in the reservoirs

The dawsonite and ankerite contents across the study area, measured on 159 thin sections, are shown in Fig. 5. Over the depths of this study (from 1841.6 m to 1868.89 m), dawsonite (0.7 to 8.3%) and ankerite (1.7 to 26.0%) in the LDX-1-1 well mainly developed near the gas water contact (GWC) (Fig. 5a). Owing to lack of samples, few observations of these minerals were made above the GWC in this well. In well LDX-1-4, the limited measurements of mineral content in the gas reservoirs show the dawsonite and ankerite content ranging from 0.7 to 2.3% and 2.0 to 14.0% above the GWC, whereas the corresponding content results for dawsonite and ankerite under the GWC in this well are 1.0 to 6.3% and 1.0 to 24.0 % (Fig. 5b).

4.4 C and O isotope compositions

The stable isotopic compositions of dawsonite and ankerite are shown in [Table 4](#) and [Fig. 6](#). The carbon isotope ($\delta^{13}\text{C}$) values for dawsonite vary from -4.3‰ to -0.6‰ with an average value of -2.0‰. The oxygen isotope ($\delta^{18}\text{O}$) values for dawsonite range from +22.4‰ to +24.0‰. The $\delta^{13}\text{C}$ values for ankerite range from -2.6‰ to -0.8‰ with an average value of -1.4‰ and the $\delta^{18}\text{O}$ values range from +22.8‰ to +23.7‰.

The measured $\delta^{13}\text{C}$ values of dawsonite and ankerite have been used to estimate the corresponding equilibrium $\delta^{13}\text{C}$ of the CO_2 ($\delta^{13}\text{C}_{\text{CO}_2}$) from which they precipitated. The $\delta^{13}\text{C}_{\text{CO}_2}$ for the CO_2 that formed the dawsonite, was estimated assuming dawsonite exhibits an identical CO_2 carbon isotope fractionation as that of calcite, using the equation proposed by [Ohmoto and Rye \(1972\)](#) ([Baker et al., 1995](#)). The calculated $\delta^{13}\text{C}$ for the CO_2 in equilibrium with ankerite was estimated assuming its fractionation was identical to the dolomite- CO_2 fractionation equation proposed by [Horita \(2014\)](#). The $\delta^{13}\text{C}$ of the CO_2 ($\delta^{13}\text{C}_{\text{CO}_2}$) calculated to be in isotopic equilibrium with dawsonite range from -9.66‰ to -6.69‰ with an average value of -7.90‰. The equilibrated $\delta^{13}\text{C}_{\text{CO}_2}$ for ankerite varies from -7.27‰ to -5.94‰ with a mean value of -6.4‰.

The formation temperature for dawsonite and ankerite were calculated from their oxygen isotope compositions. This was done by assuming oxygen fractionation between dawsonite and H_2O is identical to the calcite- H_2O fractionation equation proposed by [O'Neil et al. \(1969\)](#) and that oxygen fractionation between ankerite and H_2O is identical to the dolomite- H_2O fractionation equation of [Horita \(2014\)](#). The ^{18}O value for water used in these calculations was $\delta^{18}\text{O}_{\text{H}_2\text{O}} = +2.7\text{‰}$ ([Deng and Chen, 1994](#)), which was measured in the formation waters of the DFY-1 structure in the Yinggehai-Huangliu Formation of the Yinggehai basin ([Fig. 1](#)). The calculated temperature for dawsonite formation varies from 67.8 °C to 79.6 °C and the calculated temperature of ankerite formation ranges from 89.6 °C to 96.4 °C (see [Table 4](#)). These temperatures are consistent with 1) the earlier formation of dawsonite and 2) the increasing temperature of the study site over time as the basin subsided. Note that the current temperature of the study site is 92 to 103 °C.

5 Discussion

5.1 The origin of the carbon in the dawsonite and ankerite

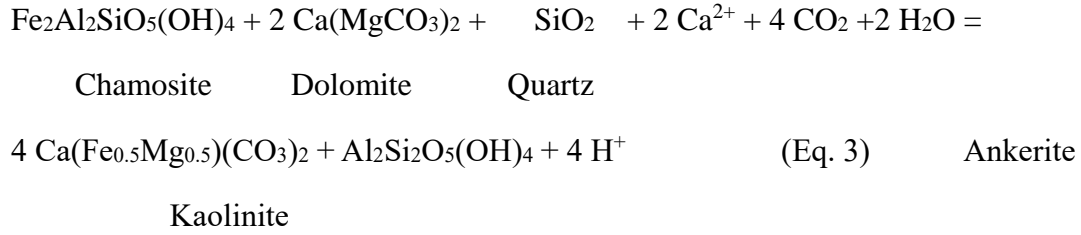
The $\delta^{13}\text{C}_{\text{CO}_2}$ of the gas forming dawsonite and ankerite reported above and in Table 4 are similar to the current $\delta^{13}\text{C}$ values in the CO_2 -rich reservoirs of the LDX system; the current $\delta^{13}\text{C}_{\text{CO}_2}$, are reported to range from -8.2‰ to -4.2‰ (He et al., 2005). Moreover, the hydrogen and oxygen isotopic compositions of the formation water in the Yinggehai Basin reservoirs are significantly different from that of meteoric water, which implies the lack of exchange between meteoric water and that present in the LDX system (Deng and Chen, 1994). Such evidence suggests that the CO_2 in the gas reservoir is likely a major carbon source for the both dawsonite and ankerite formation.

Carbon dioxide in the LDX gas reservoirs at the present time is likely dominated by magmatic derived CO_2 . Firstly, the $\delta^{13}\text{C}_{\text{CO}_2}$ value in the gas reservoir ranges from -8.2‰ to -4.2‰, which is significantly different from that obtained from kerogen degradation; $\delta^{13}\text{C}_{\text{CO}_2}$ from kerogen degradation ranges from -25‰ to -20‰ (Irwin et al., 1977; Tissot and Welte, 1984) and CO_2 from bacterial fermentation typically has a $\delta^{13}\text{C}_{\text{CO}_2} \sim +15\text{‰}$ (Irwin et al., 1977). Secondly, the carbon isotope values of CO_2 in the LDX system exhibits a $\delta^{13}\text{C}_{\text{CO}_2}$ range similar to the -8‰ to -3‰ range observed for CO_2 sourced from mantle-derived magma (Baker et al., 1995; Clayton et al., 1990; Dai, 1996; Ohmoto and Rye, 1972; Rollinson, 2014;). Taking account of the observations summarized above, we suggest that origin of the CO_2 in the LDX-1 structures is mantle-derived magma degassing.

The timing of dawsonite and ankerite formation can be constrained by the timing of the basaltic magmatism related CO_2 charging of the LDX system. The Yinggehai Formation, where the dawsonite and ankerite developed, was formed between 5.5 Ma and 1.9Ma (Fig. 2). The Honghe fault zone, which controls the formation and distribution direction of Yinggehai basin is still active (Zhu et al., 2009) (Fig. 1). The

which may be limited in this system. Note that according to mass conservation, for every 1 cm³ of dawsonite formed from albite by reaction 1, there should be 1.16 cm³ of SiO₂ precipitation (Zhou et al., 2014). However, far less microcrystalline quartz is observed in our system than dawsonite (Fig. 4b), which suggests that some of the SiO₂ may have been consumed by other water-mineral reactions.

Geochemical calculations results suggest that chlorite dissolution provoked by the charging of the system by CO₂ could provide Fe²⁺ for ankerite formation (Xu et al., 2005, 2007, 2014; Yu et al., 2014). The dissolution of smectite also could provide some of the iron for ankerite growth (Hellevang et al., 2013; Pham et al., 2011; Worden and Morad, 2003; Worden, 2006), as well as some aluminum promoting dawsonite formation. The dissolution of chlorite and smectite coupled to ankerite formation has been observed in the sandstone reservoirs of the Otway basin of Australia,, in the Songliao Basin of China, the Jurassic and late Cretaceous reservoirs of North Sea oil fields, and in the Eocene strata from Wilcox of Texas, (Awwiller, 1993; Hendry et al., 2000; Liu et al., 2011; Thyberg et al., 2010; Watson et al., 2004). The chlorite content of the Yinggehai Basin CO₂ bearing reservoirs has been reported to be significantly lower than that in CO₂-free reservoirs (Tong et al., 2012). Similar observations have been reported in wells of the Yinggehei Basin (Huang et al., 2004; Jiang et al., 2015). Such observations suggest that the dissolution of iron bearing clay minerals such as chlorite is the main Fe²⁺ source for ankerite. The Mg²⁺ and some Ca²⁺ in the ankerite crystals could come from dolomite dissolution, as fresh ankerite is observed growing within a dolomite matrix (Fig. 4i). Additional Ca²⁺ can be sourced from the transformation of clays in the system; a number of studies have reported Ca release as smectite transforms to mixed layered clays and illite (e.g. Boles and Frank, 1979; McHargue and Price, 1982). A close relation between ankerite and smectite is evident in the studied core samples (see Fig. 7). Taking account of these observations, a representative reaction coupling chlorite dissolution to ankerite precipitation could be expressed as (modified from Kirste et al., 2004; see also Luquot et al., 2012):



Note this reaction, balanced on Fe and Mg, requires substantial magmatic CO₂ for ankerite formation, consistent with its carbon isotope composition. This reaction also consumes SiO₂, which may account, at least in part, for the low mass of authigenic quartz in the present day system.

5.3 CO₂ partial pressure and carbonate mineral stability

It is likely that both ankerite and dawsonite are formed after the arrival of mantle sourced CO₂, providing a clear analogy for modern carbon capture and storage systems. The observations described in this study indicate that dawsonite is first formed at ~70 °C, followed by ankerite at ~ 90 °C, in response to the arrival of CO₂ into the overlying reservoirs. The increase in temperature in the system likely stems from its increased burial depth over time. Ankerite is also reported to be the last forming mineral in the sandstone reservoirs in Songliao (Liu et al., 2011; Yu et al., 2015) and Hailaer basins (Gao et al., 2009). Some kaolinite is seen to precipitate coupled to the dissolution of dawsonite; some dissolution etch pits on dawsonite crystal were evident near the kaolinite (Fig. 4m). Kaolinite precipitation continues as ankerite precipitates, consistent with Eq. (3). The formation of ankerite also appears to be linked to dolomite dissolution.

All of these observations are consistent with the phase diagrams shown in Figs. 8 to 10. In Fig. 8, the relative stability of dawsonite in the Na₂O-Al₂O₃-SiO₂-CO₂-H₂O system balanced on aluminum and saturated with quartz is shown. Dawsonite and quartz become stable relative to albite at log (*f*_{CO₂}) > 0.15 and 0.9 at 70 and 100 °C, respectively. This diagram thus suggests that albite would be favored to transform to dawsonite as CO₂ fills the reservoirs in accord with reaction 1. As suggested by Fig. 9,

some of the precipitated dawsonite and quartz will tend to react to form kaolinite due to an increase in temperature, which tends to shrink the dawsonite stability field. The value of $\log (f_{\text{CO}_2})$ in equilibrium with the assemblage albite = dawsonite + quartz at 70 and 100 °C plot as vertical lines on the Fig. 10, which also shows the relative stability field of ankerite + kaolinite relative to that of chlorite, dolomite and quartz consistent with reaction 3. It can be seen that for all $a_{\text{Ca}^{2+}}/a_{\text{H}^+}^2 > \sim 9.7$ at 70 °C and $> \sim 7.3$ at 100 °C, dawsonite would first tend to form before ankerite as the CO₂ partial pressure in the reservoirs increase. The partial pressure of CO₂ in the LDX system would increase as the CO₂ fraction of the gas progressively increased in the reservoirs located just above the studied rock samples (Fig. 5). The persistence of dawsonite and ankerite in this system is assured by the continued presence of the CO₂-rich gas reservoir, which maintains f_{CO_2} at relatively high levels. Note the current temperature of the gas reservoirs are 92.3 and 102.9 °C for well LDX-1-4 and well LDX-1-1 respectively, and the corresponding gas pressure in reservoirs, which is dominated by CO₂, are between 18.9 and 43.2 Mpa (China National Offshore Oil Company, personal communication). Hellevang et al. (2005), noted, that dawsonite, would likely rapidly dissolve once it became thermodynamically unstable as the f_{CO_2} decreased in the such systems.

5.4 The paragenetic sequence

Based on the observations described above, the proposed paragenetic sequence for the studied dawsonite-bearing sandstones is shown in Fig. 11. Secondary clays (mainly illite and smectite mixed layer clays) began forming before compaction during the early stage of diagenesis and coated detrital minerals as clay rims. Sideite is found to form next; siderite precipitation is readily observed in reducing, non-sulphidic pore waters in the suboxic and methanogenesis zones (Morad, 1998). Quartz overgrowths are then observed to form, perhaps due to the recrystallization of biogenic SiO₂, but also accompanied with the formation of minor kaolinite in response to feldspar dissolution.

Subsequently, dolomite is observed to form, potentially promoted by Ca and Mg release from the dissolution or transformation of the earlier formed clays. After the influx of CO₂ into the reservoir, dawsonite and additional quartz forms from the dissolution of feldspar, and subsequently ankerite and kaolinite forms from the dissolution of dolomite, quartz, chlorite and potentially some clay minerals..

5.5 Implications for carbon storage in sandstone reservoirs

The formation and long-term stability of dawsonite and ankerite in the LDX system are likely good analogies for some modern carbon storage systems such as the Shenhua CCS demonstration project in China (Yang et al., 2017). The distribution of dawsonite and ankerite in the LDX reservoirs (Fig. 5) indicates that these minerals can form in the water layers beneath gas water contact (GWC). Some dawsonite and ankerite were also observed above the present day GWC, which may indicate that either 1) the position of the GWC has changed over time or 2) that these phases grew in the gas filled section of the reservoir, potentially on water-wet surfaces. This later, process, however, is likely limited as the dawsonite and ankerite forming reactions 1 and 3 consume H₂O. The formation of such carbonate minerals adjacent to the CO₂ gas reservoir is also supported by the results of TOUGHREACT calculations reported by Pan et al. (2017) that suggest that when CO₂ is injected into sandstone reservoirs, carbonate minerals would form on both upper and lower layers of the reservoir. Carbonate mineral precipitation in the water layers below the GWC has also been observed in New Zealand sandstone reservoirs (Higgs et al., 2015). As such, we suggest that the CO₂ in the gas reservoir maintains a sufficient CO₂ partial pressure in the formation waters below the GWC to promote the growth and long term stability of dawsonite and ankerite. However, according to the paragenetic sequence determined in this study, kaolinite precipitated from the fluid concurrently with the precipitation of dawsonite and ankerite. Numerous petrographic observations and experimental simulations suggest that kaolinite and dawsonite formation could significantly reduce

sandstone permeability (Luquot et al., 2012; Shiraki and Dunn, 2000; Yu et al., 2012). Kaolinite also commonly grows in response to CO₂-feldspar or CO₂-clay mineral interaction (Luquot et al., 2012; Moore et al., 2005; Shiraki and Dunn, 2000; Yu et al., 2012). Shiraki and Dunn (2000) concluded that the precipitation and growth of kaolinite in the pores could block pore throats leading to the reduction of the permeability of reservoir. Similarly, Worden (2006) suggested that the fiber-like crystal morphology of dawsonite would also reduce sandstone permeability. The reduced permeability in the sandstone could slow chemical transport, and including potentially the transport of dissolved CO₂ out of the storage system. Such processes could thereby promote the stability of carbonate minerals in this system. The decrease in permeability could also lead to fluid pressure build up in the gas reservoir as further minerals form in this system.

6 Conclusions

This study focused on the mineral reactions provoked by the influx of CO₂ into the subarkose and sublitharenite sandstones of the Yinggehai basin. This system is likely a good analogy for subsurface carbon storage in sandstone hosted hydrocarbon reservoirs as the influxed CO₂ replaces a methane-rich gas phase in an anticlinal structure. This leads to the presence of a CO₂-rich gas phase stable over a ~1-2 million year time frame. The influx of provoked the CO₂ provoked the formation of dawsonite from plagioclase and ankerite and kaolinite likely from chlorite, quartz, and dolomite, at temperatures of 68 to 80 °C. and 90 to 96° C, respectively, largely just below the CO₂-gas water interface. The formation of such phases could provide for the mineral storage of some of the CO₂ injected during subsurface carbon storage efforts.

The key to maintaining dawsonite and ankerite stability in such systems appears to be preserving a high partial pressure of CO₂. As such, although the formation of these minerals might lead to the storage of CO₂ injected into sandstones as part of engineered geologic storage efforts, such minerals may not provide for the ‘permanent’

mineral storage of this gas that one might anticipate from the formation of carbonate minerals such as calcite, which can be stable at far lower CO₂ partial pressure, unless the system tends to become impermeable as due to the formation of various secondary minerals.

Acknowledgement

This manuscript is sponsored by the National Natural Science Foundation of China (No. 41572082), the China Scholarship Council and the project “Study on CO₂ accumulation in reservoirs and the risk assessment for key exploration regions of Chinese sea areas (No. YXKY-2015-ZY-01)” from China National Offshore Oil Corporation (CNOOC).

References

- Awwiller, D., 1993. Illite/smectite formation and potassium mass transfer during burial diagenesis of mudrocks: A study from the Texas Gulf Coast Paleocene-Eocene. *Journal of Sedimentary Research* 63(3): 501-512.
- Bachu, S., 2003. Screening and ranking of sedimentary basins for sequestration of CO₂ in geological media in response to climate change. *Environmental Geology*, 44(3): 277-289.
- Bachu, S., Gunter, W., Perkins, E., 1994. Aquifer disposal of CO₂: hydrodynamic and mineral trapping. *Energy Conversion and Management* 35(4): 269-279.
- Baker, J.C., Bai, G.P., Hamilton, P.J., Golding, S.D., Keene, J.B., 1995. Continental-scale magmatic carbon dioxide seepage recorded by dawsonite in the Bowen-Gunnedah-Sydney Basin system, eastern Australia. *Journal of Sedimentary Research* 65(3): 522-530.
- Barnes, C.S., 2006. ThermoSolver: an integrated educational thermodynamics software program. H.B. Thesis Abstr., 46p.
- Becker, R.H., 1971. Carbon and Oxygen Isotope Ratios in Iron-formation and Associated Rock from the Hammersley Range of Western Australia and Their Implications, Ph.D.Thesis University of Chicago.
- Bénézech, P., Palmer, D.A., Anovitz, L.M., Horita, J., 2007. Dawsonite synthesis and reevaluation of its thermodynamic properties from solubility measurements: Implications for mineral trapping of CO₂. *Geochimica et Cosmochimica Acta* 71(18): 4438-4455.

- Benson, S.M., Cole, D.R., 2008. CO₂ Sequestration in Deep Sedimentary Formations. *Elements* 4(5): 325-331.
- Boles, J.R., Franks, S.G., 1979. Clay diagenesis in Wilcox Sandstones of Southwest Texas: Implications of smectite diagenesis on sandstone cementation. *J. Sed. Pet.* 49(1): 55-70.
- Clayton, J., Spencer, C., Koncz, I., Szalay, A., 1990. Origin and migration of hydrocarbon gases and carbon dioxide, Bekes Basin, southeastern Hungary. *Organic Geochemistry* 15(3): 233-247.
- Comerio, M., Morosi, M.E., Tunik, M., Paredes, J.M., Zalba, P.E., 2014. The Role of Telogenetic Injection of Magmatically Derived CO₂ in the Formation of Dawsonite from the Castillo Formation, Chubut Group, Patagonia, Argentina. *The Canadian Mineralogist* 52(3): 513-531.
- Dai, J., 1996. CO₂ reservoir and its type in eastern China and continental shelf. *Nature Explore*, 15(4): 18-20 (in Chinese).
- Deng, X., Chen, M., 1994. A research on the formation water chemical characteristics in Yinggrhai basin of South China sea and its significance in petroleum geology. *Scientia Geologica Sinica* 29(4): 404-407 (in Chinese with English abstr.).
- Dickson, J., 1965. A modified staining technique for carbonates in thin section. *Nature* 205(4971): 587-587.
- Fischer, S., Liebscher, A., Wandrey, M., 2010. CO₂-brine-rock interaction — First results of long-term exposure experiments at in situ P-T conditions of the Ketzin CO₂ reservoir. *Chemie der Erde* 70: 155-164.
- Folk, R.L., 1968. *Petrology of Sedimentary rocks*. Hemphill's. Austin, Texas, 182 pp.
- Fu, M., Song, R., Xie, Y., Zhang, S., Gluyas, J., Zhang, Y., Zhang, Y., 2016. Diagenesis and reservoir quality of overpressured deep-water sandstone following inorganic carbon dioxide accumulation: Upper Miocene Huangliu Formation, Yinggehai Basin, South China Sea. *Marine and Petroleum Geology* 77: 954-972.
- Gao, Y., Liu, L., Hu, W., 2009. Petrology and isotopic geochemistry of dawsonite-bearing sandstones in Hailaer basin, northeastern China. *Applied Geochemistry* 24(9): 1724-1738.
- Gaus, I., Le Guern, C., Pearce, J., Pauwels, H., Shepherd, T., Hatziyannis, G., Metaxas, A., 2005. Comparison of long-term geochemical interactions at two natural CO₂-analogues: Montmiral (Southeast Basin, France) and Messokampos (Florina Basin, Greece) case studies, *Greenhouse Gas Control Technologies* 7. Elsevier, pp. 561-569.
- Golab, A.N., Carr, P.F., Palamara, D.R., 2006. Influence of localised igneous activity on cleat dawsonite formation in Late Permian coal measures, Upper Hunter Valley, Australia. *International Journal of Coal Geology* 66(4): 296-304.

- Gong, Z., Yang, J., Yang, Z., 1997. The major oil and gas fields of China offshore. Petroleum Industry Press, Beijing (in Chinese).
- Hao, F., Li, S., Dong, W., Hu, Z., Huang, B., 1998. Abnormal organic-matter maturation in the Yinggehai Basin, South China Sea: Implications for hydrocarbon expulsion and fluid migration from overpressured systems. *Journal of Petroleum Geology*, 21(4): 427-444.
- He, J., Xia, B., Liu, B., Zhang, S., 2005. Origin, migration and accumulation of CO₂ in East China and offshore shelf basins. *Petroleum Exploration and Development* 32(4): 663-673 (in Chinese with English abstr.).
- Hellevang, H., Aagaard, P., Oelkers, E.H., Kvamme, B., 2005. Can dawsonite permanently trap CO₂? *Environmental Science & Technology* 39(21): 8281-8287.
- Hellevang, H., Declercq, J., Aagaard, P., 2011. Why is Dawsonite Absent in CO₂ Charged Reservoirs? *Oil Gas Sci. Technol. – Rev. IFP Energies Nouvelles* 66(1): 119-135.
- Hellevang, H., Pham, V.T.H., Aagaard, P., 2013. Kinetic modelling of CO₂-water-rock interactions. *International Journal of Greenhouse Gas Control* 15: 3-15.
- Hendry, J.P., Wilkinson, M., Fallick, A.E., Haszeldine, R.S., 2000. Ankerite cementation in deeply buried Jurassic sandstone reservoirs of the central North Sea. *Journal of Sedimentary Research* 70(1): 227-239.
- Higgs, K.E., Funnell, R.H., Reyes, A.G., 2013. Changes in reservoir heterogeneity and quality as a response to high partial pressures of CO₂ in a gas reservoir, New Zealand. *Marine and Petroleum Geology* 48: 293-322.
- Higgs, K.E., Haese, R.R., Golding, S.D., Schacht, U., Watson, M.N., 2015. The Pretty Hill Formation as a natural analogue for CO₂ storage: An investigation of mineralogical and isotopic changes associated with sandstones exposed to low, intermediate and high CO₂ concentrations over geological time. *Chemical Geology* 399: 36-64.
- Hitchon, B. (Ed.), 1996. Aquifer disposal of carbon dioxide: hydrodynamic and mineral trapping-proof of concept, Geoscience Publishing, Ltd, Sherwood Park, Alberta, Canada, 165 pp
- Hoang, N., Flower, M.F., 1998. Petrogenesis of Cenozoic basalts from Vietnam: implication for origins of a ‘diffuse igneous province’. *Journal of Petrology* 39(3): 369-395.
- Hoang, N., Flower, M.F., Carlson, R.W., 1996. Major, trace element, and isotopic compositions of Vietnamese basalts: Interaction of hydrous EM1-rich asthenosphere with thinned Eurasian lithosphere. *Geochimica et Cosmochimica Acta* 60(22): 4329-4351.
- Horita, J., 2014. Oxygen and carbon isotope fractionation in the system

- dolomite-water-CO₂ to elevated temperatures. *Geochimica et Cosmochimica Acta* 129: 111-124.
- Huang, B., Li, X., Yi, P., Xiao, X., 2005. Geochemical behaviors and reservoiring history of natural gas in Ledong gas field in Yinggehai basin. *Oil and Gas Geology* 26(4): 524-529 (in Chinese with English abstr.).
- Huang, B., Xiao, X., Li, X., 2003. Geochemistry and origins of natural gases in the Yinggehai and Qiongdongnan basins, offshore South China Sea. *Organic Geochemistry* 34(7): 1009-1025.
- Huang, B., Xiao, X., Li, X., Cai, D., 2009. Spatial distribution and geochemistry of the nearshore gas seepages and their implications to natural gas migration in the Yinggehai Basin, offshore South China Sea. *Marine and Petroleum Geology* 26(6): 928-935.
- Huang, B., Xiao, X., Zhu, W., 2004. Geochemistry, origin, and accumulation of CO₂ in natural gases of the Yinggehai Basin, offshore South China Sea. *AAPG Bulletin* 88(9): 1277-1293.
- IPCC, 2005. Underground geological storage, in *Carbon dioxide capture and storage*, Metz B., Davidson O., de Coninck H., Loos M., Meyer L. (eds), Cambridge University Press, Cambridge, UK, pp. 431.
- IPCC, 2007. *Impacts, adaption and vulnerability*, Parry M.L., Canziani O.F., Palutikof J.P., van der Linden P.J., Hanson C.E. (eds), Cambridge University Press, Cambridge, UK, pp. 976.
- Irwin, H., Curtis, C., Coleman, M., 1977. Isotopic evidence for source of diagenetic carbonates formed during burial of organic-rich sediments. *Nature* 269: 209.
- Jiang, T., Xie, X., Chen, H., Wang, Z., Li, X., 2015. Geochemistry of pore water and associated diagenetic reactions in the diapiric area of Yinggehai basin, northwestern South China Sea. *Journal of Earth Science*, 26(3): 306-316.
- Johnson, J.W., Nitao, J.J., Steefel, C.I., Knauss, K.G., 2001. *Reactive Transport Modeling of Geologic CO₂ Sequestration in Saline Aquifers: The Influence of Intra-Aquifer Shales and the Relative Effectiveness of Structural, Solubility, and Mineral Trapping During Prograde and Retrograde Sequestration*, First National Conference on Carbon Sequestration. National Energy Technology Laboratory, Washington, DC.
- Klajmon, M., Havlová, V., Červinka, R., Mendoza, A., Franců, J., Berenblyum, R., Arild, Ø., 2017. REPP-CO₂: Equilibrium Modelling of CO₂-Rock-Brine Systems. *Energy Procedia* 114: 3364-3373.
- Kirste, D.M., Watson, P.R., Tingate, P.R., 2004. Geochemical modelling of CO₂-water-rock interaction in the Pretty Hill formation, Otway Basin. In Boulton, P.J., Johns, D.R., Lng, S.C. (eds.), *Eastern Australia basins symposium II*.

- Special publication 19-22, Petroleum Exploration Society of Australia, Adelaide, South Australia, pp. 404-411.
- Lackner, K.S., Wendt, C.H., Butt, D.P., Joyce, E.L., Sharp, D.H., 1995. Carbon dioxide disposal in carbonate minerals. *Energy* 20(11): 1153-1170.
- Li, C., Wang, F., Zhong, C., 2005. Geochemistry of Quaternary basaltic volcanic rocks of Weizhou island in Beihai City of Guangxi and a discussion on characteristics of their source. *Acta Petrologica et Mineralogica* 24(1): 1-11 (in Chinese with English abstr.).
- Liu, N. Liu, L., Qu, X., Yang, H., Wang, L., Zhao, S., 2011. Genesis of authigenic carbonate minerals in the Upper Cretaceous reservoir, Honggang Anticline, Songliao Basin: A natural analog for mineral trapping of natural CO₂ storage. *Sedimentary Geology* 237(3-4): 166-178.
- Luo, X., Dong, W., Yang, J., Yang, W., 2003. Overpressuring mechanisms in the Yinggehai basin, south China sea. *AAPG bulletin*, 87(4): 629-645.
- Luquot, L., Andreani, M., Gouze, P., Camps, P., 2012. CO₂ percolation experiment through chlorite/zeolite-rich sandstone (Pretty Hill Formation-Otway Basin-Australia). *Chemical Geology* 294-295: 75-88.
- McCrea, J.M., 1950. On the isotopic chemistry of carbonates and a paleotemperature scale. *The Journal of Chemical Physics* 18(6): 849-857.
- McHargue, T.R., Price, R.C., 1982. Dolomite from clay in argillaceous or shale-associated marine carbonates. *J. Sed. Pet.* 52(3): 873-886.
- Manabe, S., Stouffer, R.J., 1993. Century-scale effects of increased atmospheric CO₂ on the ocean-atmosphere system. *Nature*, 364(6434): 215-218.
- Matter, J.M., Stute, M., Snæbjörnsdóttir, S.Ó., Oelkers, E.H., Gislason, S.R., Aradóttir, E.S., Sigfusson, B., Gunnarsson, I., Sigurdardóttir, H., Gunnlaugsson, E., Axelsson, G., Alfredsson, H.A., Wolff-Boenisch, D., Mesfin, K., Fernandez de la Reguera Tayà, D., Hall, J., Dideriksen, K. and Broecker, W.S. (2016) Rapid carbon mineralization for permanent disposal of anthropogenic carbon dioxide emissions. *Science* 352: 1312-1314
- Meng, F., Xiao, L., Xie, Y., Wang, Z., Liu, J., Tong, C., Zhang, H., Gao, Y., Meng, Y., Wei, W., 2012. Abnormal Transformation of the Clay Minerals in Yinggehai Basin and Its Significances. *Acta Sedimentologica Sinica* 30(3): 469-476 (in Chinese with English abstr.).
- Ming, X., Liu, L., Yu, L., Bai, H., Yu, Z., Liu, N., Yang, H., Wang, F., Li, B., 2017. Thin-film dawsonite in Jurassic coal measure strata of the Yaojie coalfield, Minhe Basin, China: A natural analogue for mineral carbon storage in wet supercritical CO₂. *International Journal of Coal Geology* 180: 83-99.
- Moore, J., Adams, M., Allis, R., Lutz, S., Rauzi, S., 2005. Mineralogical and

- geochemical consequences of the long-term presence of CO₂ in natural reservoirs: An example from the Springerville-St. Johns Field, Arizona, and New Mexico, U.S.A. *Chemical Geology* 217(3-4): 365-385.
- Morad, S., 1998. Carbonate cementation in sandstones: distribution patterns and geochemical evolution. In: Morad, S. (Ed.), *Carbonate Cement in Sandstone Reservoirs*. Special Publication of the International Association of Sedimentologists, 26, pp. 1–26.
- O'Neil, J.R., Clayton, R.N., Mayeda, T.K., 1969. Oxygen isotope fractionation in divalent metal carbonates. *The Journal of Chemical Physics* 51(12): 5547-5558.
- Oelkers, E.H., Cole, D.R., 2008. Carbon dioxide sequestration a solution to a global problem. *Elements* 4(5): 305-310.
- Oelkers, E.H., Gislason, S.R., Matter, J., 2008. Mineral Carbonation of CO₂. *Elements* 4(5): 333-337.
- Ohmoto, H., Rye, R., 1972. Isotopes of sulfur and carbon. In *Geochemistry of Hydrothermal Ore Deposits* (ed. H. L. Barnes), pp. 509-567. John Wiley, New York.
- Pan, F., McPherson, B.J., Kaszuba, J., 2017. Evaluation of CO₂-Fluid-Rock Interaction in Enhanced Geothermal Systems: Field-Scale Geochemical Simulations. *Geofluids* 2017: 1-11.
- Parkhurst, D.L., Appelo, C., 2013. Description of input and examples for PHREEQC version 3--A computer program for speciation, batch-reaction, one-dimensional transport, and inverse geochemical calculations. U.S. Geol. Surv. Techniques Methods 6-A43, 497 p. <<http://pubs.usgs.gov/tm/06/a43>>.
- Pauwels, H., Gaus, I., Le Nindre, Y.M., Pearce, J., Czernichowski-Lauriol, I., 2007. Chemistry of fluids from a natural analogue for a geological CO₂ storage site (Montmiral, France): lessons for CO₂-water-rock interaction assessment and monitoring. *Applied Geochemistry* 22(12): 2817-2833.
- Pearce, J.K., Dawson, G.K.W., Law, A.C.K., Biddle, D., Golding, S.D., 2016. Reactivity of micas and cap-rock in wet supercritical CO₂ with SO₂ and O₂ at CO₂ storage conditions. *Applied Geochemistry* 72: 59-76.
- Pham, V.T.H., Lu, P., Aagaard, P., Zhu, C., Hellevang, H., 2011. On the potential of CO₂-water-rock interactions for CO₂ storage using a modified kinetic model. *International Journal of Greenhouse Gas Control* 5(4): 1002-1015.
- Power, I.M., Harrison, A.L., Dipple, G.M., Wilson, S.A., Kelemen, P.B., Hitch, M., Southam, G., 2013. Carbon mineralization: from natural analogues to engineered systems. *Reviews in Mineralogy and Geochemistry* 77(1): 305-360.
- Rollinson, H., 2014. *Using geochemical data: evaluation, presentation, interpretation*. Routledge, Interpretation. Longman, London. 352 pp.

- Rosenbaum, J., Sheppard, S., 1986. An isotopic study of siderites, dolomites and ankerites at high temperatures. *Geochimica et Cosmochimica Acta*, 50(6): 1147-1150.
- Ryzhenko, B., 2006. Genesis of dawsonite mineralization: Thermodynamic analysis and alternatives. *Geochemistry International* 44(8): 835-840.
- Sharma, T., Clayton, R.N., 1965. Measurement of O^{18}/O^{16} ratios of total oxygen of carbonates. *Geochimica et Cosmochimica Acta* 29(12): 1347-1353.
- Shiraki, R., Dunn, T.L., 2000. Experimental study on water-rock interactions during CO_2 flooding in the Tensleep Formation, Wyoming, USA. *Applied Geochemistry* 15(3): 265-279.
- Sun, Y., Wang, Y., 2000. Main gas sources and gas charge history in Yinggehai-Qiongdongnan region. *China Offshore Oil And Gas (Geology)* 14(4): 240-247 (in Chinese with English abstr.).
- Thyberg, B., Jahren, J., Winje, T., Bjørlykke, K., Faleide, J.I., Marcussen, Ø., 2010. Quartz cementation in Late Cretaceous mudstones, northern North Sea: Changes in rock properties due to dissolution of smectite and precipitation of micro-quartz crystals. *Marine and Petroleum Geology* 27(8): 1752-1764.
- Tissot, B.P., Welte, D.H., 1984. From kerogen to petroleum, *Petroleum formation and occurrence*. Springer, pp. 160-198.
- Tong, C., Wang, Z., Li, X., 2012. Pooling conditions of gas reservoirs in the Dongfang 1-1 Gas Field, Yinggehai Basin. *Natural Gas Industry* 32(8): 11-15 (in Chinese with English abstr.).
- Uysal, I.T., Golding, S.D., Bolhar, R., Zhao, J., Feng, Y., Baublys, K.A., Greig, A., 2011. CO_2 degassing and trapping during hydrothermal cycles related to Gondwana rifting in eastern Australia. *Geochimica et Cosmochimica Acta* 75(19): 5444-5466.
- Van Pham, T.H., Aagaard, P., Hellevang, H., 2012. On the potential for CO_2 mineral storage in continental flood basalts-PHREEQC batch-and 1D diffusion-reaction simulations. *Geochemical Transactions* 13(1): 5.
- Wan, Z., Xia, B., He, J., Liu, B., 2007. The comparative study of hydrocarbon accumulation conditions in Yinggehai and Qiongdongnan basins, Northern South China Sea. *Natural Gas Geoscience* 18(5): 648-652 (in Chinese with English abstr.).
- Wang, J., Yin, A., Harrison, T.M., Grove, M., Zhang, Y., Xie, G., 2001. A tectonic model for Cenozoic igneous activities in the eastern Indo-Asian collision zone. *Earth and Planetary Science Letters* 188(1): 123-133.
- Wang, Z., He, J., Xie, X., 2004. Heat flow action and its control on natural gas migration and accumulation in mud-fluid diapir areas in Yinggehai basin. *Earth*

- Science 29(2): 203-210 (in Chinese with English abstr.).
- Wang, Z., Huang, B., 2008. Dongfang 1-1 gas field in the mud diapir belt of the Yinggehai Basin, South China Sea. *Marine and Petroleum Geology* 25(4): 445-455.
- Watson, M.N., Zwingmann, N., Lemon, N.M., 2004. The Ladbroke Grove-Katnook carbon dioxide natural laboratory: A recent CO₂ accumulation in a lithic sandstone reservoir. *Energy* 29(9-10): 1457-1466.
- Worden, R., Morad, S., 2003. Clay minerals in sandstones: A review of the detrital and diagenetic sources and evolution during burial. *Clay Mineral Cement in Sandstones* 34: 3-41.
- Worden, R.H., 2006. Dawsonite cement in the Triassic Lam Formation, Shabwa Basin, Yemen: A natural analogue for a potential mineral product of subsurface CO₂ storage for greenhouse gas reduction. *Marine and Petroleum Geology* 23(1): 61-77.
- Xi, K., Cao, Y., Zhu, R., Haile, B.G., Hellevang, H., 2016. Evidences of localized CO₂-induced diagenesis in the Cretaceous Quantou Formation, southern Songliao Basin, China. *International Journal of Greenhouse Gas Control* 52: 155-174.
- Xie, Y., Zhang, Y., Xu, D., Gan, J., 2014. Natural gas origin and accumulation model in major and excellent gas fields with high temperature and overpressure in Yinggehai basin: a case of DF13-2 gas field. *China Offshore Oil and Gas* 26(2): 1-5 (in Chinese with English abstr.).
- Xu, T., Apps, J.A., Pruess, K., 2004. Numerical simulation of CO₂ disposal by mineral trapping in deep aquifers. *Applied Geochemistry* 19(6): 917-936.
- Xu, T., Apps, J.A., Pruess, K., 2005. Mineral sequestration of carbon dioxide in a sandstone-shale system. *Chemical Geology* 217(3-4): 295-318.
- Xu, T., Apps, J.A., Pruess, K., Yamamoto, H., 2007. Numerical modeling of injection and mineral trapping of CO₂ with H₂S and SO₂ in a sandstone formation. *Chemical Geology* 242(3-4): 319-346.
- Xu, T., Feng, G., Shi, Y., 2014. On fluid-rock chemical interaction in CO₂-based geothermal systems. *Journal of Geochemical Exploration* 144: 179-193.
- Xu, T., Kharaka, Y.K., Doughty, C., Freifeld, B.M., Daley, T.M., 2010. Reactive transport modeling to study changes in water chemistry induced by CO₂ injection at the Frio-I Brine Pilot. *Chemical Geology* 271(3-4): 153-164.
- Yu, M., Liu, L., Yu, Z., Liu, N., Yang, H., Qu, X., 2014. Dawsonite fixation of mantle CO₂ in the cretaceous Songliao Basin, Northeast China: a natural analogue for CO₂ mineral trapping in oilfields. *International Geology Review* 56(14): 1792-1812.
- Yang, G., Li, Y., Atrens, A., Liu, D., Wang, Y., Jia, L., Lu, Y., 2017. Reactive transport

- modeling of long-term CO₂ sequestration mechanisms at the Shenhua CCS demonstration project, *China Journal of Earth Science*, 28(3): 457-472.
- Yu, Z., Liu, L., Liu, K., Yang, S., Yang, Y., 2015. Petrological characterization and reactive transport simulation of a high-water-cut oil reservoir in the Southern Songliao Basin, Eastern China for CO₂ sequestration. *International Journal of Greenhouse Gas Control* 37: 191-212.
- Yu, Z., Liu, L., Yang, S., Li, S., Yang, Y., 2012. An experimental study of CO₂-brine-rock interaction at in situ pressure-temperature reservoir conditions. *Chemical Geology* 326-327: 88-101.
- Zhao, S., Liu, L., Liu, N., 2018. Petrographic and stable isotopic evidences of CO₂-induced alterations in sandstones in the Lishui sag, East China Sea Basin, China. *Applied Geochemistry* 90: 115-128.
- Zhou, B., Liu, L., Zhao, S., Ming, X., Oelkers, E.H., Yu, Z., Zhu, D., 2014. Dawsonite formation in the Beier Sag, Hailaer Basin, NE China tuff: A natural analog for mineral carbon storage. *Applied Geochemistry* 48: 155-167.
- Zhu, B., Wang, H., 1989. Nd-Sr-Pb isotopic and chemical evidence for the volcanism with MORB-OIB source characteristics in the Leiqiong area. *Geochimica* 3: 193-201 (in Chinese with English abstr.).
- Zhu, M., Graham, S., McHargue, T., 2009. The Red River Fault zone in the Yinggehai Basin, South China Sea. *Tectonophysics* 476(3-4): 397-417.
- Zhu, W., Wu, G., Li, M., 2004. Palaeolimology and hydrocarbon potential in Beibu gulf basin of South China Sea. *Oceanologia et Limnologia Sinica* 35(1): 8-14 (in Chinese with English abstr.).
- Zhu, W., Zhang, G., Yang, S., 2007. North continental margin basin in the south China sea. *Petroleum Industry Press Beijing* (in Chinese).
- Zimmer, K., Zhang, Y., Lu, P., Chen, Y., Zhang, G., Dalkilic, M., Zhu, C., 2016. SUPCRTBL: A revised and extended thermodynamic dataset and software package of SUPCRT92. *Computers & Geosciences* 90: 97-111.

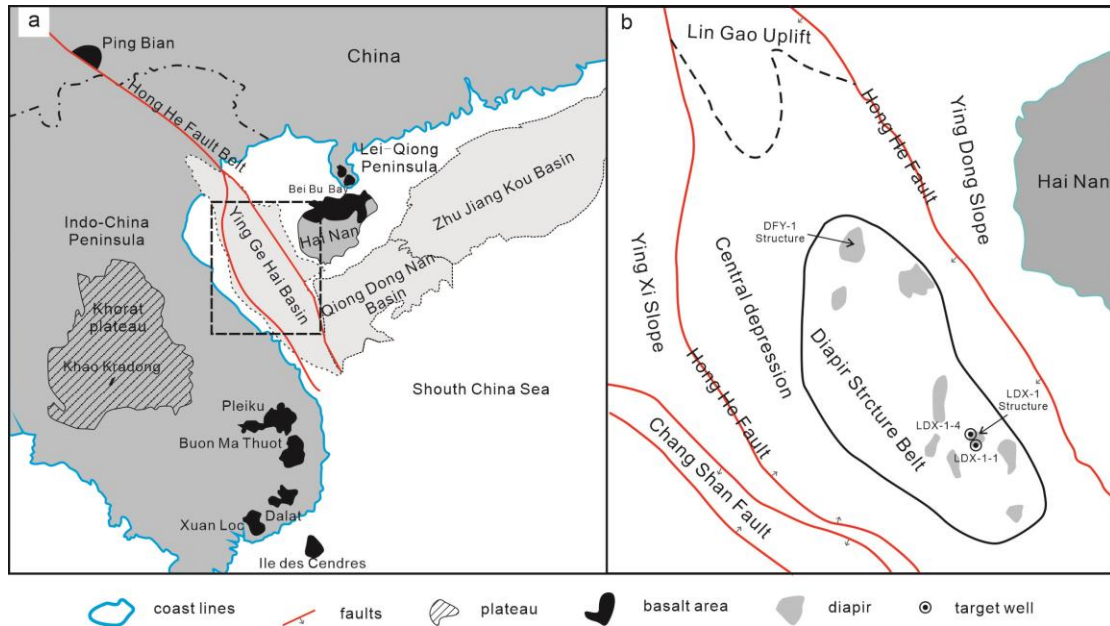


Figure 1. Location map of LDX-1 structure in Yinggehai Basin, south China Sea area. a) The location of Yinggehai basin and basalt area modified after Shi and Yan (2011), basalt areas are modified from Hoang et al. (1996, 1998), Li et al. (2005), Wang et al. (2001); Zhou et al. (1997) and Zhu et al. (1989), b) Geotectonic units modified after Luo et al., (2003) and Meng et al. (2012).

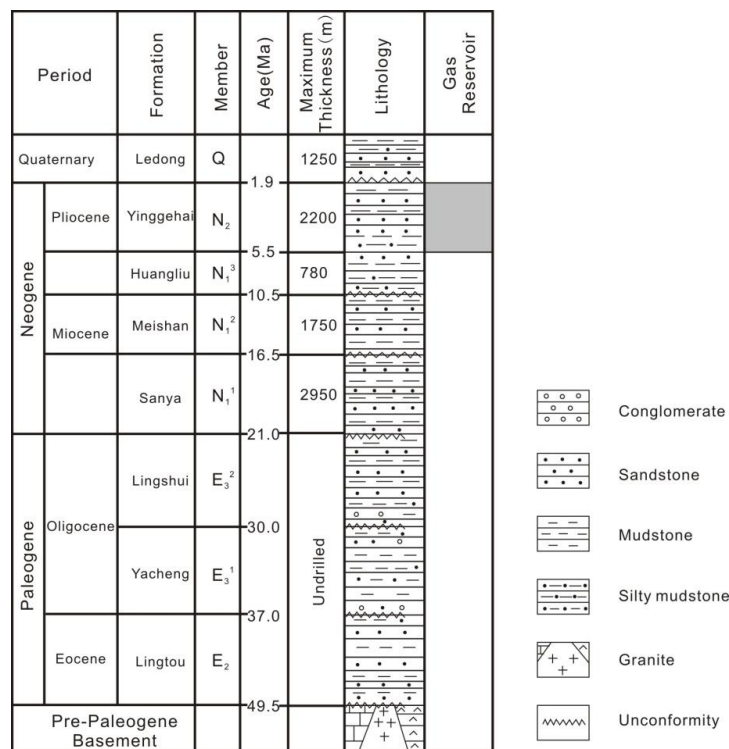


Figure 2. Simplified stratigraphic column of the Yinggehai basin modified after Gong et al. (1997) and Huang et al. (2003).

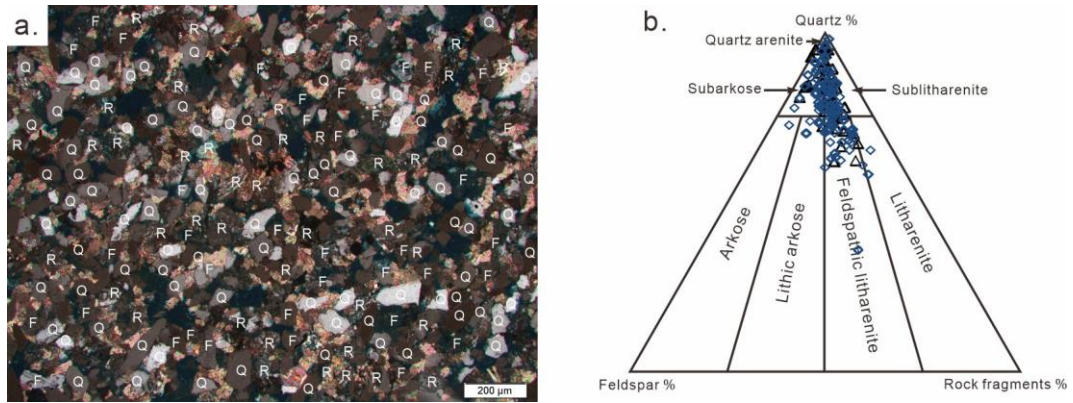


Figure 3. a) Image of a thin section of a sandstone sample collected from a depth of 1860.72 m in the LDX-1-1 well showing its detrital minerals: Q=quartz, F=feldspar and R=rock fragment. b) Mineral composition diagram, after Folk (1968), of the dawsonite-bearing samples from well LDX-1-1 (blue rhombuses) and well LDX-1-4 (black triangles). All the data were obtained through point-counting - see text.

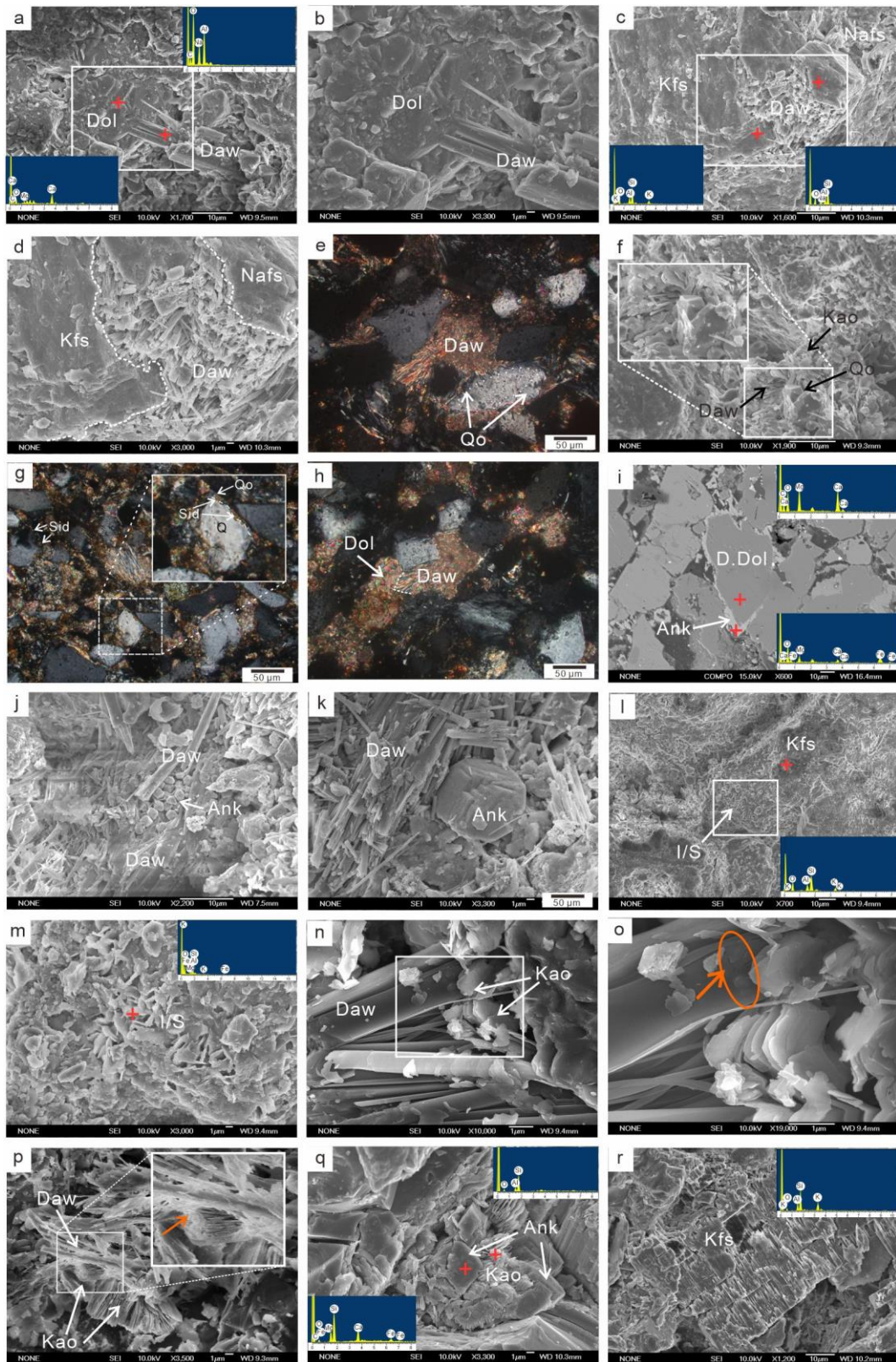


Figure 4. Micrographs of diagenetic minerals. (a, b) Acicular dawsonite growing on top of dolomite (red crosses are EDS probe spots), SEM; (c, d) Dawsonite replacing feldspar and plagioclase with EDS analysis results (red crosses are EDS probe spots); (e) Dawsonite replacing quartz overgrowths, thin section micrograph, cross polar; (f) Microcrystalline quartz grows with kaolinite on the top of drusy dawsonite, SEM; (g) Siderite surrounding detrital

minerals and on the inner side of quartz overgrowths, thin section micrograph, cross polar; (h) Dawsonite replacing dolomite (dashed line), thin section micrograph, cross polar; (i) Ankerite enclosing and replacing dolomite (red crosses are EDS probe spots), BSM; (j) rhombic-like ankerite with dawsonite in the pores, SEM; (k) the growth of rhombic-like ankerite adhering the dawsonite, SEM; (l, m) honeycombed-like illite and smectite mixed layer coating on detrital K-feldspar (red crosses are EDS probe spots), SEM; (n) kaolinite growing on drusy dawsonite, SEM; (o) Magnification of white box area in figure (n), some tiny etch pits are observed (red arrow, in the red circle) on dawsonite potentially caused by the growth of kaolinite, SEM; (p) Acicular dawsonite overlying (red crosses) kaolinite aggregation; (q) ankerite formed on the top of kaolinite aggregation (red crosses are EDS probe spots), SEM; (r) dissolution of K-feldspar and EDS results, SEM image. Qo: quartz overgrowth; Daw: dawsonite; Kao: kaolinite; Sid: siderite; Dol: dolomite; C: Detrital dolomite Ank: ankerite; I/S: illite and smectite mixed layer; Kfs: K-feldspar; Nafs: Na-feldspar.

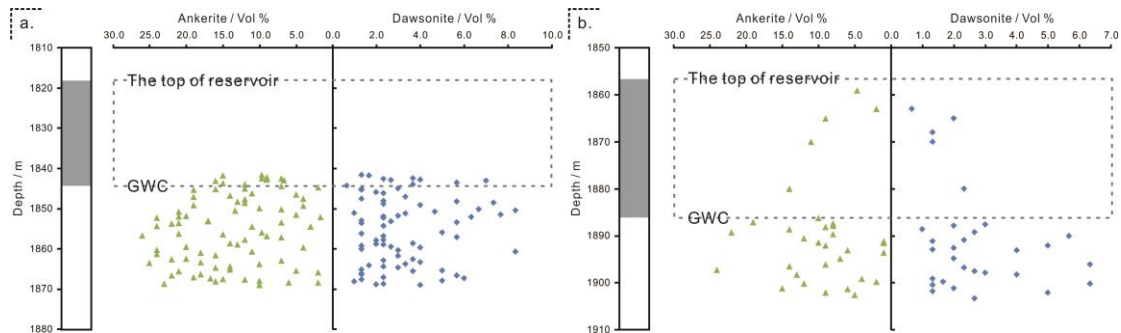


Figure 5. Plot of volume percent versus depth for dawsonite (blue rhombuses) and ankerite (green triangles) in well LDX-1-1 (Fig 3a) and well LDX-1-4 (Fig 3b). The filled gray areas and dashed boxes indicate the location of gas layers, the water layers in the reservoir system are below the gas layers. The gas-water-contact (GWC), as reported by the China National Offshore Oil Company are located at 1844.1m and 1886.0m depth in wells LDX-1-1 and LDX-1-4, respectively.

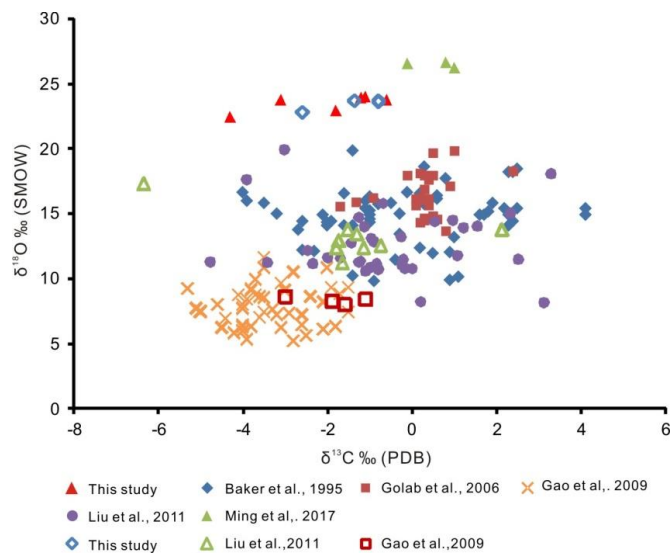


Figure 6. Plot of $\delta^{13}\text{C}$ versus $\delta^{18}\text{O}$ values for dawsonite and ankerite samples. Filled symbols represent the compositions of dawsonite, and open symbols for ankerite. The filled red triangles and open blue rhombus correspond to compositions measured in this study from the LDX-1 structure, Yinggehai basin, China. Compositions of dawsonite from the Bowen-Gunnedah-Sydney basin system in Australia reported by Baker et al. (1995) are shown as filled blue rhombuses, those from the late Permian coal measures of the Upper Hunter Valley in Australia reported by Golab et al. (2006) are shown as filled dark red squares, those of the Cretaceous Hailaer basin in China reported by Gao et al. (2009) are shown as filled yellow crosses, those of the upper Cretaceous Songliao Basin in China reported by Liu et al. (2011) are shown as filled purple circles, and those of the Yaojie coalfield, Minhe basin in China reported by Ming et al. (2017) are shown as filled green triangles. Compositions of ankerite from the Cretaceous Hailaer basin in China reported by Gao et al. (2009) are shown as open red squares, and those of the upper Cretaceous Honggang anticline of the Songliao Basin in China reported by Liu et al. (2011) are shown as open green triangles.

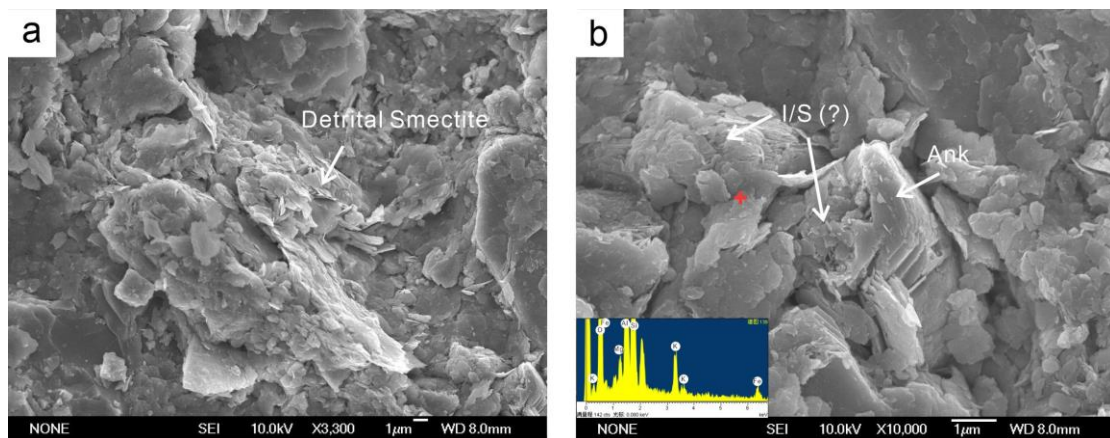


Figure 7. Images of clay minerals observed in this study. (a) detrital smectite in the sandstone and (b) image showing the relationship between smectite and ankerite. Rhombic ankerite crystals grew and adhered to the mixed layer of illite/smectite, suggesting the transformation of smectite could provide some of the materials for ankerite. I/S: mixed

layer of illite/smectite; Ank: ankerite.

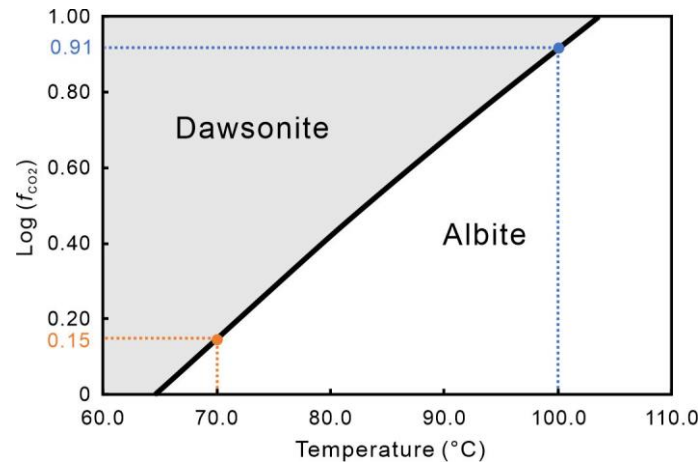


Figure 8 Log fugacity of CO₂ ($\log(f_{\text{CO}_2})$) versus temperature (°C) diagram depicting mineral stability fields in the system Na₂O-Al₂O₃-SiO₂-CO₂-H₂O balanced on Al and at quartz equilibrium. The grey area indicates the stability field of dawsonite, and the white area indicates the stability field for albite. The orange and blue lines highlight the $\log(f_{\text{CO}_2})$ values in equilibrium with dawsonite and albite at 70 and 100 °C, respectively. This figure was generated using PHREEQC together with its llnl database – see text.

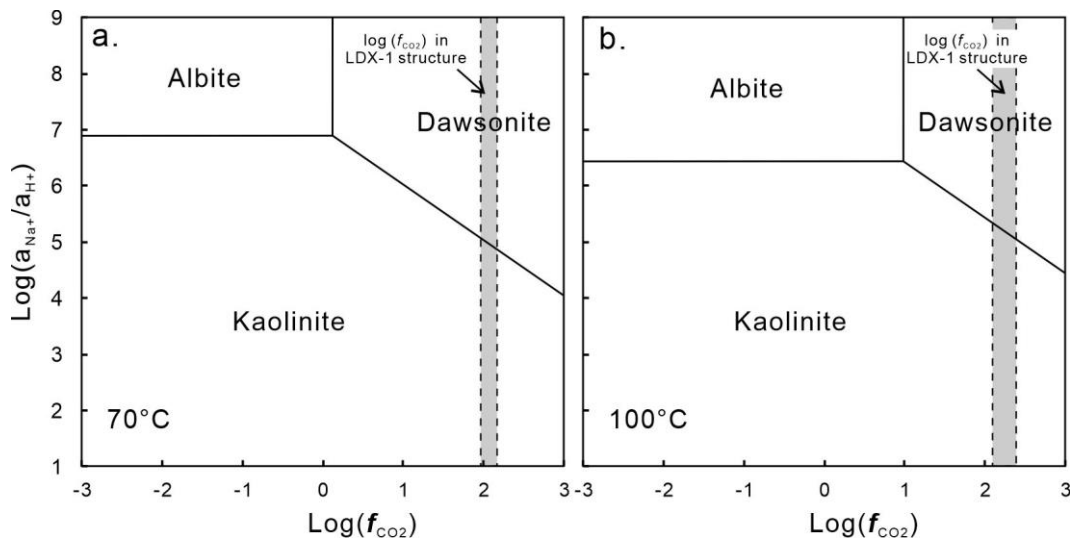


Figure 9. Log fugacity of CO₂ ($\log(f_{\text{CO}_2})$) versus $\log a_{\text{Na}^+}/a_{\text{H}^+}$ diagrams depicting mineral stability fields in the system Na₂O-Al₂O₃-SiO₂-CO₂-H₂O balanced on Al and at quartz equilibrium at 70 °C and 100 °C. The dashed area represents the current $\log(f_{\text{CO}_2})$ range in the reservoirs considered in this study. This figure was generated using PHREEQC together with its llnl database – see text.

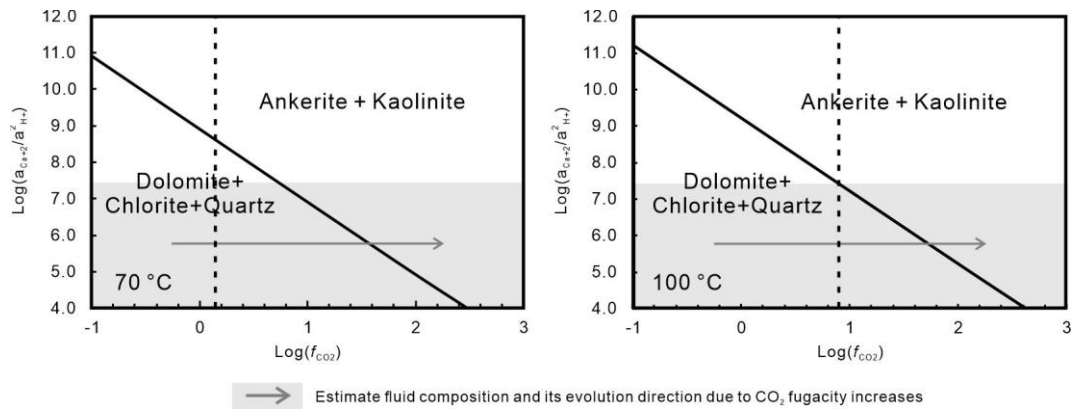


Figure 10. Phase diagram of $\log \text{CO}_2$ fugacity ($\log (f_{\text{CO}_2})$) versus $\log a_{\text{Ca}^{2+}}/a_{\text{H}^{+}}^2$. The dashed vertical lines correspond to equilibrium compositions of reaction 1, whereas the sloped lines correspond to equilibrium compositions of reaction 3. The grey area is the likely aqueous activity ratio of $a_{\text{Ca}^{2+}}/a_{\text{H}^{+}}^2$ in the studied system and the arrow illustrates the direction of the CO_2 fugacity evolution in the system as the reservoir fills with CO_2 . This figure was generated using PHREEQC together with its *llnl* database after adding estimated values for the thermodynamics properties of ankerite— see text.

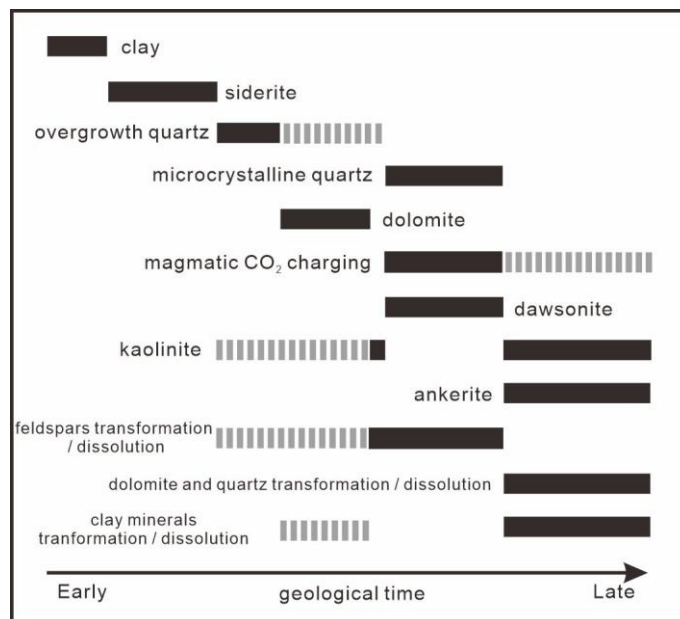


Figure 11. Paragenetic sequence for dawsonite-bearing sandstones in this study. The black bars are indicated by petrologic observations, the grey dashed bars are estimated based on the mass balance considerations and reactions (1) and (3).

Table 1. EDS analysis data for dawsonite.

Well	Weight Percentage, %					Atomic Percentage, %				
	C	Na	Al	O	Si	C	Na	Al	O	Si
LDX-1-1	18.76	4.98	12.99	63.27	n.d.	25.14	3.48	7.75	63.63	n.d.
LDX-1-1	15.88	11.13	14.19	58.8	n.d.	22.01	8.06	8.76	61.18	n.d.
LDX-1-1	11.81	12.44	12.96	55.55	7.23	17.14	9.44	8.38	60.55	4.49
LDX-1-4	14.88	13.8	14.24	57.09	n.d.	20.87	10.11	8.89	60.13	n.d.
LDX-1-4	15.61	12.53	13.7	58.15	n.d.	21.71	9.11	8.48	60.7	n.d.
LDX-1-4	12.62	14.69	17.98	54.72	n.d.	18.19	11.06	11.54	59.21	n.d.
LDX-1-4	12.64	8.37	14.29	57.5	7.2	18.15	6.28	9.14	62	4.43
LDX-1-4	7.83	6.83	8.83	55.28	21.23	11.88	5.41	5.96	62.97	13.78
LDX-1-4	12.58	12.01	19.97	55.44	n.d.	18.13	9.04	12.82	60.01	n.d.
LDX-1-4	9.14	14.68	24.74	51.45	n.d.	13.75	11.54	16.57	58.13	n.d.
LDX-1-1	10.16	13.06	23.91	52.87	n.d.	15.09	10.13	15.81	58.96	n.d.
LDX-1-1	11.59	9.4	23.75	55.26	n.d.	16.9	7.16	15.42	60.52	n.d.
LDX-1-1	18.76	4.98	12.99	63.27	n.d.	25.14	3.48	7.75	63.63	n.d.
LDX-1-1	11.97	10.19	18.04	55.91	3.88	17.36	7.72	11.64	60.86	2.41
LDX-1-1	7.25	12.06	30.26	50.43	n.d.	11.18	9.71	20.76	58.35	n.d.

LDX-1-1	13.42	13.99	16.92	55.67	n.d.	19.16	10.43	10.75	59.66	n.d.
LDX-1-1	13.68	13.29	16.93	56.11	n.d.	19.46	9.88	10.72	59.94	n.d.
LDX-1-1	18.6	7.9	11.21	62.28	n.d.	24.98	5.54	6.7	62.78	n.d.
LDX-1-1	12.75	11.24	20.18	55.83	n.d.	18.34	8.45	12.92	60.29	n.d.
LDX-1-1	10.17	12.49	24.3	53.04	n.d.	15.1	9.69	16.07	59.14	n.d.
LDX-1-4	13.71	7.2	12.99	58.84	7.26	19.43	5.33	8.2	62.63	4.4
LDX-1-4	11.98	13.11	16.51	55.02	3.38	17.39	9.93	10.66	59.92	2.1
LDX-1-4	10.86	13.85	21.98	53.31	n.d.	16	10.65	14.41	58.94	n.d.
LDX-1-4	22.23	3.58	7.27	66.93	n.d.	28.65	2.41	4.17	64.77	n.d.
LDX-1-4	10.18	12.73	24.1	52.99	n.d.	15.12	9.88	15.93	59.07	n.d.
LDX-1-4	12.26	13.58	19.45	54.7	n.d.	17.75	10.27	12.53	59.44	n.d.

n.d.: not be detected.

Table 2. EDS analysis data for ankerite

Well	Weight Percent								Atomic Percent							
	C	O	Na	Mg	Al	Si	Ca	Fe	C	O	Na	Mg	Al	Si	Ca	Fe
LDX-1-4	9.66	51.32	n.d.	6.54	n.d.	4.42	6.29	21.77	16.14	64.34	n.d.	5.4	n.d.	3.16	3.15	7.82
LDX-1-4	13.15	52.72	n.d.	8.46	n.d.	n.d.	19.73	5.95	20.52	61.75	n.d.	6.52	n.d.	n.d.	9.22	2
LDX-1-4	10.3	53.98	n.d.	7.09	n.d.	1.77	17.26	9.6	16.53	65.02	n.d.	5.62	n.d.	1.22	8.3	3.31
LDX-1-4	12.96	57.98	n.d.	5.16	2.28	1.72	1.12	18.77	19.89	66.79	n.d.	3.92	1.56	1.13	0.52	6.2
LDX-1-4	16.52	61.57	n.d.	7.64	n.d.	n.d.	0.92	13.35	23.71	66.35	n.d.	5.42	n.d.	n.d.	0.39	4.12
LDX-1-4	12.79	61.42	n.d.	6.25	1.52	2.56	2.73	12.73	19	68.49	n.d.	4.59	1	1.62	1.21	4.07
LDX-1-4	15.63	55.85	n.d.	3.64	1.34	4.16	11.59	7.79	23.37	62.69	n.d.	2.69	0.89	2.66	5.19	2.5
LDX-1-1	13.97	59.87	1.84	5.04	1.69	0.84	12.09	4.66	20.51	66	1.41	3.66	1.1	0.53	5.32	1.47
LDX-1-1	13.39	59.42	n.d.	5.56	n.d.	2.16	12.7	6.78	20.01	66.65	n.d.	4.1	n.d.	1.38	5.69	2.18
LDX-1-1	12.41	60.07	n.d.	3.29	2.27	11.6	3.16	7.2	18.36	66.71	n.d.	2.4	1.49	7.34	1.4	2.29
LDX-1-1	10.25	45.23	n.d.	3.86	2.24	5.18	16.05	17.17	17.73	58.71	n.d.	3.3	1.73	3.83	8.32	6.39

n.d.: not be detected.

Table 3. EDS analysis data for smectite and the mixed layer of illite and smectite

Well	Weight Percentage, %									Atomic Percentage, %								
	C	O	Na	Mg	Al	Si	K	Ca	Fe	C	O	Na	Mg	Al	Si	K	Ca	Fe
LDX-1-1	3.31	57	2.64	0.63	6.64	26.9	1.24	0.37	1.27	5.25	67.91	2.19	0.49	4.69	18.26	0.6	0.18	0.43
LDX-1-1	n.d.	41.41	n.d.	1.22	9.69	35.81	6.72	n.d.	5.14	n.d.	57.05	n.d.	1.11	7.92	28.11	3.79	n.d.	2.03
LDX-1-1	n.d.	37.5	n.d.	1.55	9.06	39.51	4.7	n.d.	7.67	n.d.	53.18	n.d.	1.44	7.62	31.92	2.73	n.d.	3.12
LDX-1-1	n.d.	47.11	1.39	1.93	14.08	26.38	2.12	n.d.	6.99	n.d.	62.32	1.28	1.68	11.04	19.88	1.15	n.d.	2.65
LDX-1-4	n.d.	57.17	0.7	0.99	15.27	22.26	2.53	n.d.	1.08	n.d.	70.24	0.6	0.8	11.13	15.58	1.27	n.d.	0.38
LDX-1-4	n.d.	54.36	n.d.	4.31	8.23	11.71	n.d.	13.46	7.93	n.d.	71.16	n.d.	3.71	6.38	8.73	n.d.	7.03	2.98
LDX-1-4	n.d.	52.97	n.d.	1.18	13.35	26.82	4.82	n.d.	0.87	n.d.	66.92	n.d.	0.98	10	19.3	2.49	n.d.	0.31
LDX-1-4	n.d.	55.21	n.d.	1.52	11.51	27.18	1.39	n.d.	3.18	n.d.	69.01	n.d.	1.25	8.53	19.35	0.71	n.d.	1.14
LDX-1-4	n.d.	45.84	n.d.	1.44	14.38	28.31	3.13	n.d.	6.91	n.d.	61.37	n.d.	1.27	11.42	21.59	1.71	n.d.	2.65
LDX-1-4	n.d.	46.01	n.d.	1.67	12.96	29.18	2.94	n.d.	7.24	n.d.	61.6	n.d.	1.47	10.29	22.25	1.61	n.d.	2.78
LDX-1-4	n.d.	46.45	n.d.	1.52	15.13	26.85	4.9	n.d.	5.16	n.d.	61.77	n.d.	1.33	11.93	20.34	2.67	n.d.	1.96
LDX-1-4	n.d.	52.5	n.d.	1.34	13.43	26.4	2.83	n.d.	3.49	n.d.	66.84	n.d.	1.12	10.14	19.15	1.48	n.d.	1.27
LDX-1-4	n.d.	52.32	1.04	1.26	9.4	29.16	1.99	n.d.	3.28	n.d.	66.71	0.92	1.05	7.11	21.18	1.04	0.79	1.2
LDX-1-4	n.d.	39.97	n.d.	1.14	10.55	39.83	2.53	n.d.	4.37	n.d.	55.06	n.d.	1.04	8.62	31.26	1.43	0.87	1.73
LDX-1-4	n.d.	32.01	n.d.	0.97	12.81	34.05	12.63	n.d.	7.54	n.d.	47.8	n.d.	0.95	11.34	28.97	7.72	n.d.	3.23
LDX-1-4	n.d.	53.67	0.98	0.99	11.99	28.2	2.38	n.d.	1.8	n.d.	67.37	0.86	0.82	8.92	20.16	1.22	n.d.	0.65
LDX-1-1	n.d.	53.91	n.d.	1.68	12.75	25.32	4.2	n.d.	2.13	n.d.	67.96	n.d.	1.4	9.53	18.18	2.17	n.d.	0.77
LDX-1-1	n.d.	61.56	1.25	0.99	9.68	22.71	2.14	n.d.	1.68	n.d.	74.07	1.04	0.79	6.9	15.56	1.05	n.d.	0.58
LDX-1-1	n.d.	63.93	1.67	2.62	8.94	16.76	1.11	n.d.	4.97	n.d.	76.52	1.39	2.06	6.35	11.43	0.54	n.d.	1.7
LDX-1-1	n.d.	35.98	n.d.	1.82	11.82	35.41	8.01	n.d.	6.96	n.d.	51.68	n.d.	1.72	10.07	28.97	4.7	n.d.	2.86

n.d.: not be detected.

Table 4. Carbon and oxygen isotopic compositions for dawsonite and ankerite

Well	Depth	Mineral	$\delta^{13}\text{C}$	$\delta^{18}\text{O}$	$\delta^{18}\text{O}$	Isotopic temp.	$\delta^{13}\text{C}_{\text{CO}_2}$
	m		‰, PDB	‰, PDB	‰, SMOW	°C	‰, PDB
LDX-1-4	1894.8	Dawsonite	-1.2	-6.8	23.9	68.53	-7.39
LDX-1-4	1896.07	Dawsonite	-1.1	-6.7	24.0	67.83	-7.34
LDX-1-4	1897.57	Dawsonite	-0.6	-7.0	23.7	69.94	-6.69
LDX-1-4	1900.2	Dawsonite	-1.8	-7.8	22.9	75.76	-7.44
LDX-1-1	1842.5	Dawsonite	-4.3	-8.3	22.4	79.56	-9.66
LDX-1-1	1863.34	Dawsonite	-3.1	-7.0	23.7	69.94	-9.17
LDX-1-4	1889.07	Ankerite	-2.6	-7.8	22.8	96.44	-7.27
LDX-1-4	1894.8	Ankerite	-0.8	-7.0	23.7	89.56	-5.94
LDX-1-4	1897.57	Ankerite	-0.8	-7.1	23.6	90.31	-5.88
LDX-1-4	1900.2	Ankerite	-1.4	-7.0	23.7	89.56	-6.50